


Article

Morphology of Barite Synthesized by In-Situ Mixing of Na₂SO₄ and BaCl₂ Solutions at 200 °C

Chunyao Wang^{1,2}, Li Zhou^{3,4,*} , Shuai Zhang^{1,2}, Li Wang¹, Chunwan Wei⁵, Wenlei Song^{6,7}, Liping Xu⁸ and Wenge Zhou^{1,*}

- ¹ Key Laboratory of High-Temperature and High-Pressure Study of the Earth's Interior, Institute of Geochemistry, Chinese Academy of Sciences, Guiyang 550081, China; wangchunyao@mail.gyig.ac.cn (C.W.); shuaizhang19950902@163.com (S.Z.); wangli19940204@foxmail.com (L.W.)
- ² College of Earth and Planetary Sciences, University of Chinese Academy of Sciences, Beijing 100049, China
- ³ School of Geography and Environmental Science, Guizhou Normal University, Guiyang 550025, China
- ⁴ State Key Laboratory Incubation Base for Karst Mountain Ecology Environment of Guizhou Province, Guiyang 550001, China
- ⁵ Key Laboratory of Orogenic Belts and Crustal Evolution, School of Earth and Space Sciences, Peking University, Beijing 100871, China; cwwei@pku.edu.cn
- ⁶ State Key Laboratory of Continental Dynamics, Department of Geology, Northwest University, Xi'an 710069, China; wlsong@nwu.edu.cn
- ⁷ BIC Brno, Technology Innovation Transfer Chamber, 61200 Brno, Czech Republic
- ⁸ School of Fundamental Science, Zhejiang Pharmaceutical College, No. 666 Siming Road, Ningbo 315500, China; xulp@zjpu.edu.cn
- * Correspondence: zhouli@gznu.edu.cn (L.Z.); zhouwenge@mail.gyig.ac.cn (W.Z.)



Citation: Wang, C.; Zhou, L.; Zhang, S.; Wang, L.; Wei, C.; Song, W.; Xu, L.; Zhou, W. Morphology of Barite Synthesized by In-Situ Mixing of Na₂SO₄ and BaCl₂ Solutions at 200 °C. *Crystals* **2021**, *11*, 962. <https://doi.org/10.3390/cryst11080962>

Academic Editor: Vladislav V. Gurzhiy

Received: 8 July 2021

Accepted: 14 August 2021

Published: 16 August 2021

Publisher's Note: MDPI stays neutral with regard to jurisdictional claims in published maps and institutional affiliations.



Copyright: © 2021 by the authors. Licensee MDPI, Basel, Switzerland. This article is an open access article distributed under the terms and conditions of the Creative Commons Attribution (CC BY) license (<https://creativecommons.org/licenses/by/4.0/>).

Abstract: Barite is an abundant sulfate mineral in nature. Especially, the variety of morphologies of barite is often driven by the mixing of Ba-bearing hydrothermal fluid and sulfate-bearing seawater around hydrothermal chimneys. In order to better understand the factors affecting the morphology and precipitation mechanism(s) of barite in seafloor hydrothermal systems, we synthesized barite by a new method of in-situ mixing of BaCl₂ and Na₂SO₄ solutions at 200 °C while varying Ba concentrations and ratios of Ba²⁺/SO₄²⁻, and at room temperature for comparison. The results show that barite synthesized by in-situ mixing of BaCl₂ and Na₂SO₄ solutions at 200 °C forms a variety of morphologies, including rod-shaped, granular, plate-shaped, dendritic, X-shaped, and T-shaped morphologies, while room temperature barites display relatively simple, granular, or leaf-like morphologies. Thus, temperature affects barite morphology. Moreover, dendritic barite crystals only occurred at conditions where Ba²⁺ is in excess of SO₄²⁻ at the experimental concentrations. The dendritic morphology of barite may be an important typomorphic feature of barite formed in high-temperature fluids directly mixing with excess Ba²⁺ relative to SO₄²⁻.

Keywords: Barite; hydrothermal synthesis; typomorphic characteristics; in-situ mixing solutions at high temperature

1. Introduction

Barite (BaSO₄) is a ubiquitous mineral in the earth's crust [1,2]. Early Earth's marine environments were anoxic and sulfate deposits prevailed, resulting in barite as the dominant or the only sulfate mineral within bedded sulfate deposits older than 2.4 Ga [3–7]. Due to its high density and strong resistance to chemical weathering, barite is present throughout Earth's history and has the potential to preserve a record of conditions attending formation, which could be useful for interpretations of Earth's ancient rocks and paleoenvironments [8].

There are many ways of forming natural barite, including magmatic, biogenic, and hydrothermal genesis. Magmatic barite has been found in the Mianning rare earth deposit, Sichuan, Southwestern China [9]. In this deposit, barite is believed to have formed

prior to or at the same time as massive quartz and fluorite, in the late stages of magma crystallization [10]. Biogenic barite occurs in various sedimentary environments, generally by combining barium with the skeletons of plankton [11,12]. Hydrothermal barite forms by the reaction of ore-forming hydrothermal fluids with surrounding rock [13,14]. Moreover, hydrothermal barite is the most abundant mineral in seafloor sulfate-sulfide deposits formed in back-arc basins, such as Kuroko, Mariana, and Okinawa deposits [15]. In-depth studies of the deposition mechanisms of sulfate and sulfide minerals in these deposits show that barite is formed by the rapid mixing of Ba^{2+} -containing hydrothermal fluid with the surrounding SO_4^{2-} -rich seawater [16–19]. For example, barite in the hydrothermal vent of the Endeavour Segment, Juan de Fuca Ridge has a variety of morphologies, including plate, leaf, needle, or radiating cone shapes, and dendritic crystals [19].

On the other hand, many experimental studies on the precipitation of barite from aqueous solution have been carried out to investigate the precipitation kinetics of barite in hydrothermal environments [15,20–25]. The results show that the morphology of barite varies greatly, depending on many factors. However, in previous experiments, barium-bearing solutions and sulfate-bearing solutions were mixed at room temperature, before heating to the desired temperature for crystal growth. This process is quite different from the process of barite precipitation from hydrothermal fluids since barite is believed to be formed by mixing a Ba^{2+} -bearing solution with an SO_4^{2-} -bearing solution at high temperatures in natural hydrothermal systems [19]. Therefore, the previous experimental results may not be directly applicable to the precipitation of barite in hydrothermal vents.

In order to better simulate the formation process of barite, and better understand the factors affecting the morphology and precipitation mechanisms of barite in seafloor hydrothermal solutions, we synthesized barite by in-situ mixing of barium-bearing and sulfate-bearing solutions of variable concentrations and mixing ratios of $\text{Ba}^{2+}/\text{SO}_4^{2-}$ at 200 °C and discuss the effects of different mixing ratios of barium and sulfate solutions on the morphology of barite. We also compare the morphologies of barites synthesized by in-situ mixing of Na_2SO_4 and BaCl_2 solutions at 200 °C with those grown at room temperature.

2. Materials and Methods

2.1. Materials

The reagents, anhydrous sodium sulfate (Na_2SO_4 , 99.99%, metals basis) and barium chloride dihydrate ($\text{BaCl}_2 \cdot 2\text{H}_2\text{O}$, 99.99%, metals basis), used in the experiments are all produced by Shanghai Aladdin Biochemical Technology Co., Ltd. Solutions were prepared with ultra-pure water. An SO_4^{2-} concentration similar to that of seawater (0.03 mol/kg) was chosen. In addition, to investigate the effect of concentration on barite precipitation, a higher concentration of SO_4^{2-} (0.1 mol/kg) was also prepared. Ba^{2+} solutions of similar concentration (0.03 mol/kg and 0.1 mol/kg) were also prepared.

2.2. Experimental Methods

Hydrothermal synthesis is a common method of synthesis [26–28]. Rather than mixing solutions at room temperature and then heating them to high temperatures for crystal growth, this study synthesized barite by a new method of in-situ mixing of BaCl_2 and Na_2SO_4 solutions at 200 °C. The experiments utilized conventional stainless steel autoclaves with two Teflon bottle linings (Figure 1a). The height of the stainless steel autoclave is 70 mm and the diameter is 45 mm, while the heights of the outer Teflon bottle and the inner bottle are 55 mm and 30 mm, with diameters of 32 mm and 15 mm, respectively. The filling degree of the whole equipment is 47%. The sodium sulfate solution was first added to the inner Teflon bottle, and the barium chloride solution was added to the outer Teflon bottle, then the Teflon lining with these separated solutions was sealed within the stainless steel autoclave. The stainless steel autoclave with these starting solutions was maintained vertically while in the electric furnace to avoid solutions mixing at temperatures lower than 200 °C. After the temperature was raised to 200 °C and maintained for one hour, the

electric furnace was rotated from vertical to horizontal, allowing the solutions in the inner and outer bottles to mix in-situ at 200 °C (Figure 1b). All experiments were kept at 200 °C for 7 days. At the end of the experiment, the power was cut off and the run product was quenched. Note that our pre-experiment results showed that no barite was observed in the solutions in the inner and outer bottles when keeping the temperature at 200 °C for 7 days without rotation. Therefore, the barite produced in the high-temperature rotation experiment was formed by in-situ mixing of solutions at high temperatures.

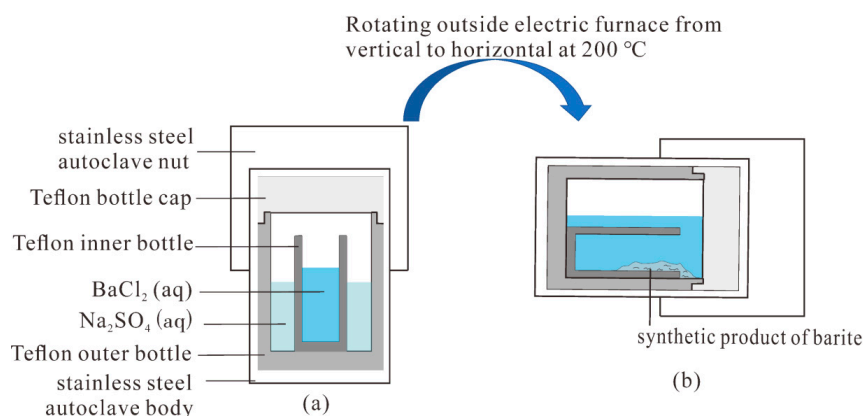


Figure 1. Simple diagram of synthetic equipment. (a) before mixing at 200 °C (b) after mixing at 200 °C.

After quenching and cooling, the solution and products in the Teflon bottle were poured into the centrifugal tube and centrifuged to extract the precipitate. Then the precipitate was washed three times alternately with deionized water and anhydrous ethanol. Finally, the white precipitate was dried at 60 °C to obtain a white powder.

For the mixing experiments at room temperature, different mixing ratios of sodium sulfate solution and barium chloride solution were added into the Teflon bottle and stirred evenly to produce a white precipitate, and then the mixed solution was kept at room temperature for 7 days. The purification of the product used the same procedure as that of the in-situ mixing experiments at 200 °C.

We carried out 10 experiments of in-situ mixing of Na₂SO₄ and BaCl₂ solutions at 200 °C and 10 experiments of mixing solutions at room temperature with 5 solution mixing ratios at two initial concentrations. The experimental conditions are shown in Table 1.

Table 1. The experimental conditions.

Sample	Solution Mixing Ratio (Molar Ratio of Na ₂ SO ₄ to BaCl ₂)	SO ₄ ²⁻ (mol/kg)	Ba ²⁺ (mol/kg)	T(°C)
1	8:2	0.03	0.03	200
2	7:3	0.03	0.03	200
3	1:1	0.03	0.03	200
4	3:7	0.03	0.03	200
5	2:8	0.03	0.03	200
6	8:2	0.1	0.1	200
7	7:3	0.1	0.1	200
8	1:1	0.1	0.1	200
9	3:7	0.1	0.1	200
10	2:8	0.1	0.1	200
11	8:2	0.03	0.03	Room temperature
12	7:3	0.03	0.03	Room temperature
13	1:1	0.03	0.03	Room temperature
14	3:7	0.03	0.03	Room temperature
15	2:8	0.03	0.03	Room temperature
16	8:2	0.1	0.1	Room temperature
17	7:3	0.1	0.1	Room temperature
18	1:1	0.1	0.1	Room temperature
19	3:7	0.1	0.1	Room temperature
20	2:8	0.1	0.1	Room temperature

2.3. Analytical Methods

A Renishaw inVia Reflex spectrometer system equipped with a standard confocal microscope was used for Raman spectral analysis at the Institute of Geochemistry, Chinese Academy of Sciences. A Renishaw diode-pumped solid-state laser provided 532 nm laser excitation with 5 mW power at the sample. An 1800 grooves/mm grating was used giving a spectral resolution of 1.2 cm^{-1} . Depolarized Raman spectra were obtained using 10 s integration times with 5 accumulations and a $50\times$ Leica long working distance microscope objective, which focused the beam to a spot size of $1.6 \mu\text{m}$. Wavenumber calibration was carried out using a silicon standard.

The scanning electron microscope (SEM) images were obtained using an FEI- Scanning Electron Microscope with Scios Dual Beam System at the Institute of Geochemistry, Chinese Academy of Sciences. The instrument was operated at an acceleration voltage of 5–20 kV, a beam current of 0.2–0.4 nA, and a working distance of 7–10 mm. The sample was dispersed in alcohol, dropped onto conductive glue, coated with gold, and then analyzed by a scanning electron microscope.

Powder X-ray diffraction analyses of barite were carried out using an Empyrean diffractometer (Malvern Panalytical) at the Institute of Geochemistry, Chinese Academy of Sciences. The maximum power of the cermet X-ray tube (Cu target) was 2.2 kW; the minimum step of the goniometer was 0.0001° , and the working current was 40 mA, scanning speed was $10^\circ/\text{min}$, and the scanning range was $10\text{--}70^\circ$. The data obtained were analyzed with Jade software, and unit cell parameters were obtained.

3. Results

3.1. Morphology of Barite Synthesized by In-Situ Mixing of Solutions at 200°C

As shown in Figure 2, barite synthesized using 5 mixing ratios of Na_2SO_4 and BaCl_2 solutions by in-situ mixing at 200°C produced six different morphologies, including rod-shaped, granular, plate-shaped, dendritic, X-shaped, and T-shaped crystals. The specific morphologies appearing in the mixed solution of different proportions are shown in Table 2.

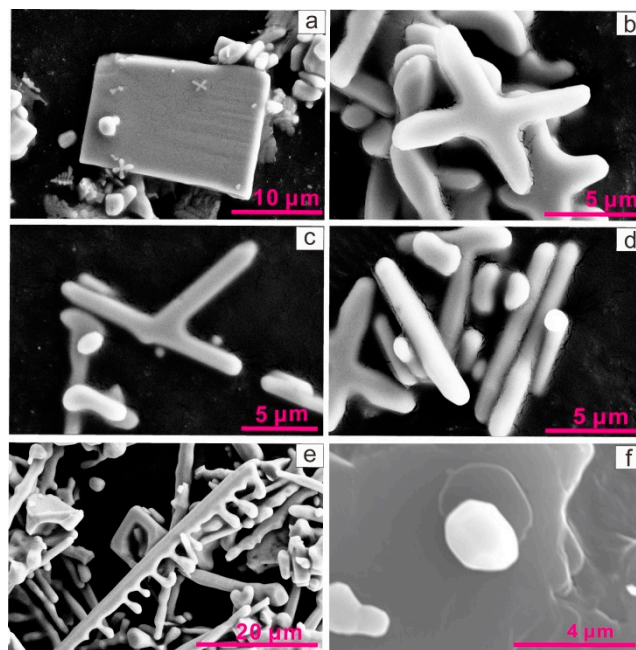


Figure 2. Scanning electron microscope (SEM) images of barite synthesized by in situ mixing of Na_2SO_4 and BaCl_2 solutions at 200°C . (a) plate-shaped (b) X-shaped (c) T-shaped (d) rod-shaped (e) dendritic (f) granular.

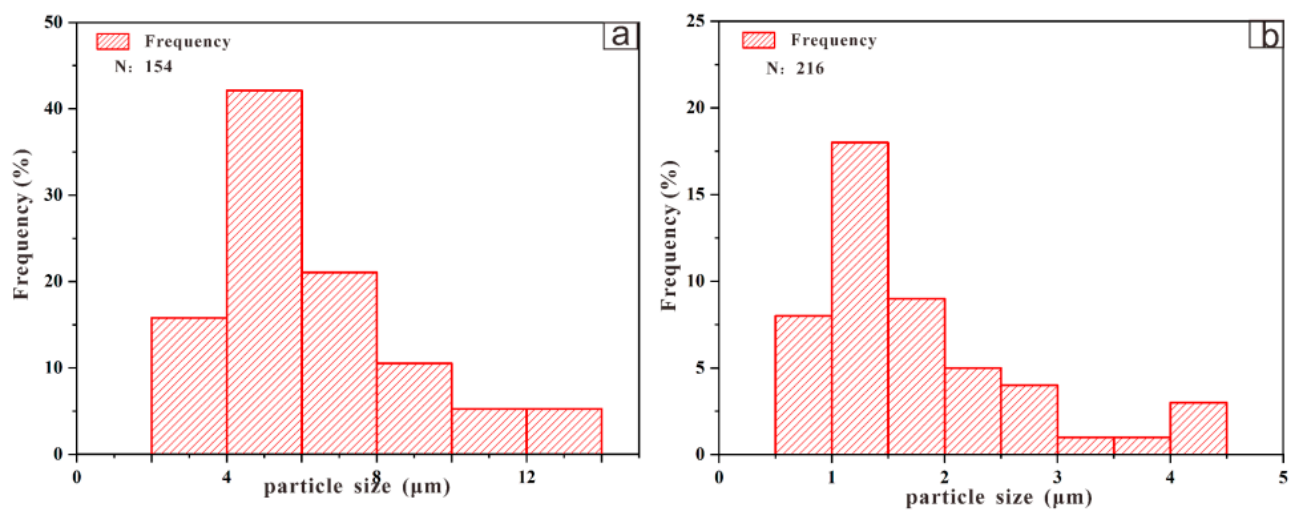
Table 2. The morphological statistics of barite appearing in a mixed solution of barium salt and sulfate with different ratios at 200 °C.

Synthetic Condition	Solution Mixing Ratio (Molar Ratio of Na ₂ SO ₄ to BaCl ₂)	Morphology of Barite					
		Rod-Shaped	Granular	Plate-Shaped	Dendritic	X-Shaped	T-Shaped
0.03 mol/kg Na ₂ SO ₄ and BaCl ₂	8:2	+	+	-	-	+	+
	7:3	+	+	-	-	+	+
	1:1	+	+	+	-	+	+
	3:7	+	+	+	-	+	+
	2:8	+	+	+	+	+	+
0.1 mol/kg Na ₂ SO ₄ and BaCl ₂	8:2	+	+	-	-	+	+
	7:3	+	+	-	-	+	+
	1:1	+	+	+	-	+	+
	3:7	+	+	+	+	+	+
	2:8	+	+	+	+	+	+

Note: "+" indicates existence and "-" indicates absence.

At concentrations of Na₂SO₄ and BaCl₂ solutions of 0.03 mol/kg, rod-shaped, granular, X-shaped, and T-shaped crystals appeared in all mixing ratios, while plate-shaped crystals appeared in the mixes of 1:1, 3:7, and 2:8 and dendritic shapes only appeared in mixes of 2:8. In addition, at concentrations of Na₂SO₄ and BaCl₂ of 0.1 mol/kg, rod-shaped, granular, X-shaped, and T-shaped crystals appeared in all 5 mixing proportions, while plate-shaped crystals appeared in the mixes of 1:1, 3:7, and 2:8, and dendritic appeared in the mixes of 3:7 and 2:8.

The histograms of the barite particle size synthesized in mixes of 0.03 mol/kg Na₂SO₄ and BaCl₂ with a ratio of 2:8 at 200 °C are shown in Figure 3. The plate-shaped barite with a particle size of 4.0–6.0 µm accounts for about 42% of the total, the rod-shaped barite with a particle size of 1.0–1.5 µm accounts for about 18% of the total, the granular barite with a particle size of 2.0–2.5 µm accounts for about 39% of the total, the dendritic barites with a particle size in the range of 1.5–2.0 µm and 2.0–2.5 µm account for about 26% of the total, respectively, the T-shaped barite with a particle size in the range of 3.0–4.0 µm and 4.0–5.0 µm account for about 33% of the total, respectively, and the X-shaped barite with a particle size of 5.0–6.0 µm accounts for about 33% of the total.

**Figure 3.** Cont.

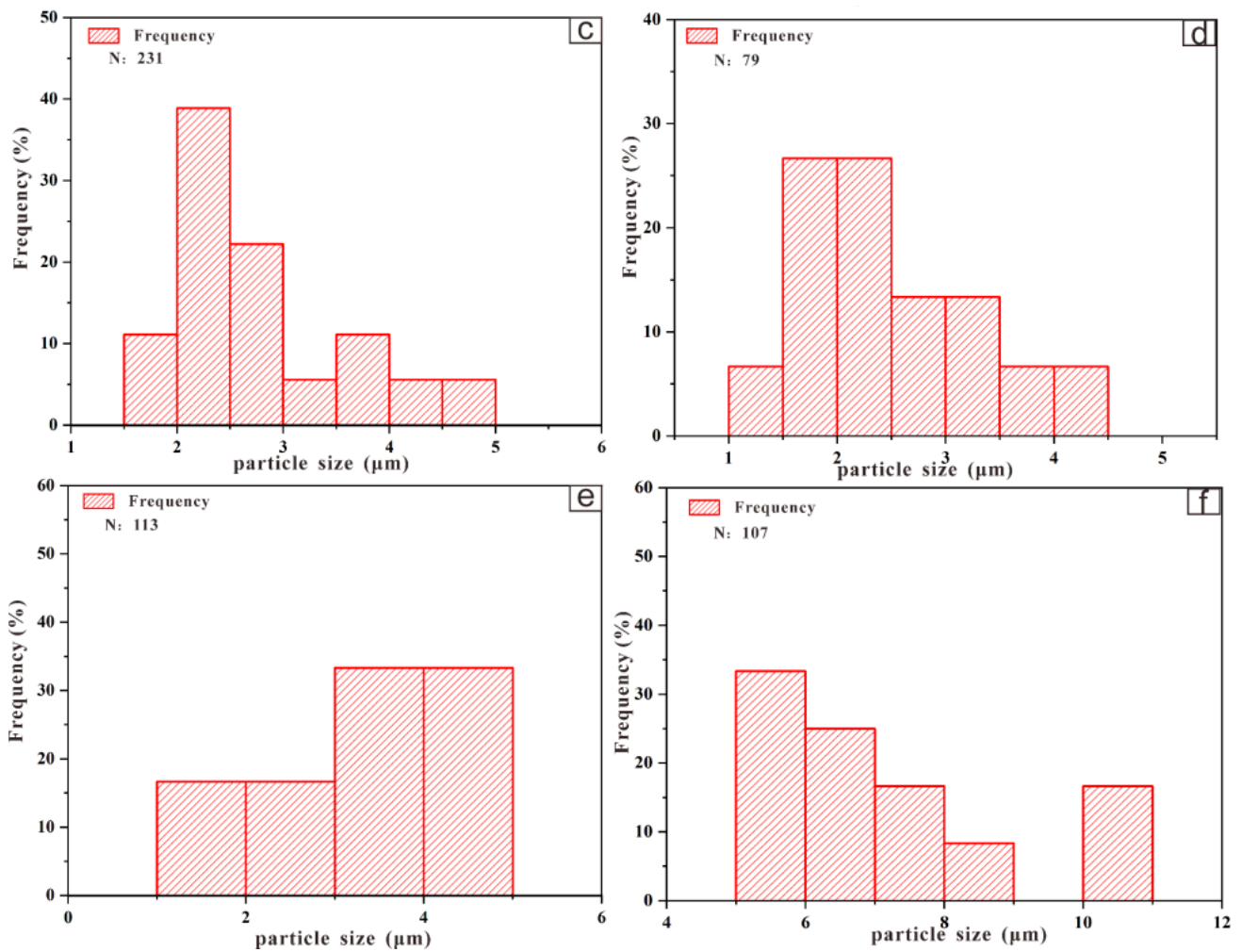


Figure 3. Histograms of the barite particle size with different morphology. The barite was synthesized using a mixed solution of 0.03 mol/kg Na_2SO_4 and BaCl_2 with a ratio of 2:8 at 200 °C. (a) plate-shaped (b) rod-shaped (c) granular (d) dendritic (e) T-shaped (f) X-shaped. N: statistic.

3.2. Morphology of Barite Synthesized at Room Temperature

When the initial ion concentration is constant, the morphologies of the barite synthesized at room temperature with different mixing ratios are the same, and the change of the mixing ratio does not change barite morphology (Figure 4). The morphology of barite is leaf-like when the initial concentration of Na_2SO_4 and BaCl_2 solution is 0.03 mol/kg; the morphology of barite consists of nanospheres when the initial concentration of Na_2SO_4 and BaCl_2 solution is 0.1 mol/kg. And the particle size distribution of barite synthesized by mixed solutions at room temperature shows a normal distribution (Figure 5).

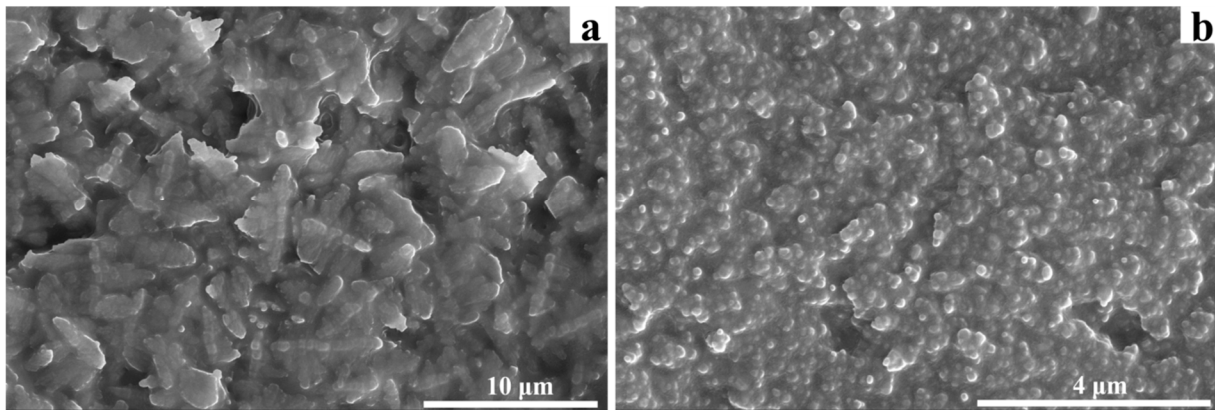


Figure 4. Scanning electron microscope (SEM) images of barite synthesized with a mixed solution of 0.03 mol/kg Na_2SO_4 and BaCl_2 (a) and a mixed solution of 0.1 mol/kg Na_2SO_4 and BaCl_2 (b) with a ratio of 1:1 at room temperature.

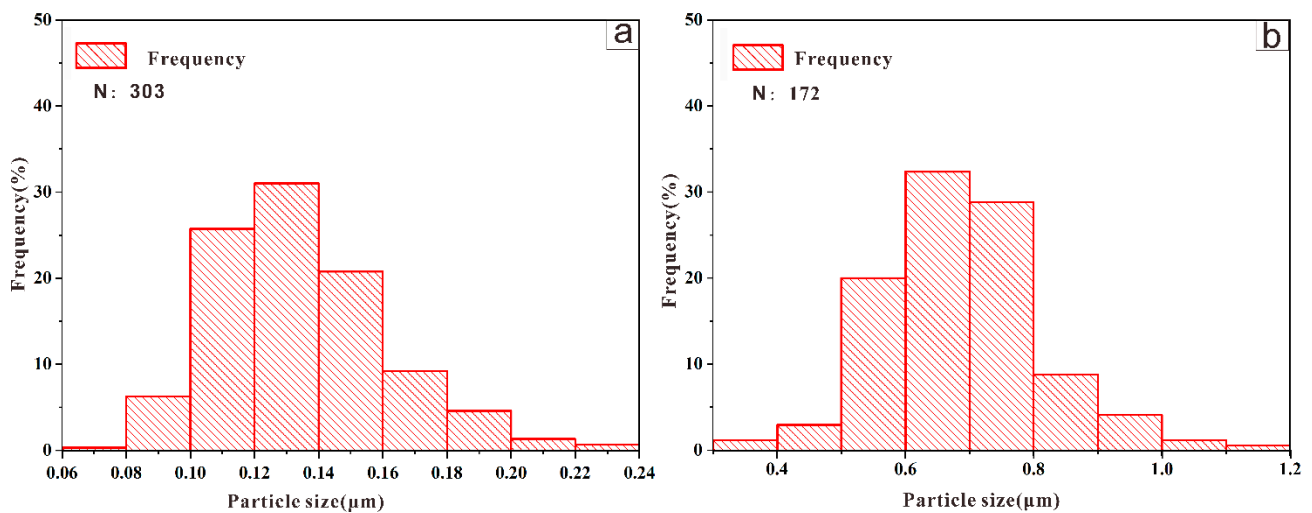


Figure 5. Histograms of barite particle size synthesized using a mixed solution of 0.1 mol/kg Na_2SO_4 and BaCl_2 (a) and a mixed solution of 0.03 mol/kg Na_2SO_4 and BaCl_2 (b) with a mixing ratio of 1:1 at room temperature. N: statistic.

3.3. Raman Spectra

The Raman spectra of barite synthesized at room temperature and 200 °C are shown in Figure 6. The structure of barite is orthorhombic, of the Pbnm space group [29]. Each S atom coordinates with four oxygen atoms to form SO_4 tetrahedra while each Ba^{2+} coordinates with 12 oxygen atoms. The SO_4 tetrahedra have Cs site group symmetry which theoretically has 9 degrees of vibrational freedom [30] (i.e., one nondegenerate (ν_1), one doubly degenerate (ν_2), and two triply degenerate modes (ν_3 and ν_4)). Moreover, one additional mode at 1104 cm^{-1} caused by SO_4 tetrahedral distortion remained unassigned in this study. The Raman peaks below 400 cm^{-1} are classified as Ba- O_{12} vibrations. The observed patterns are consistent with those reported previously [31,32] and are listed in Table 3.

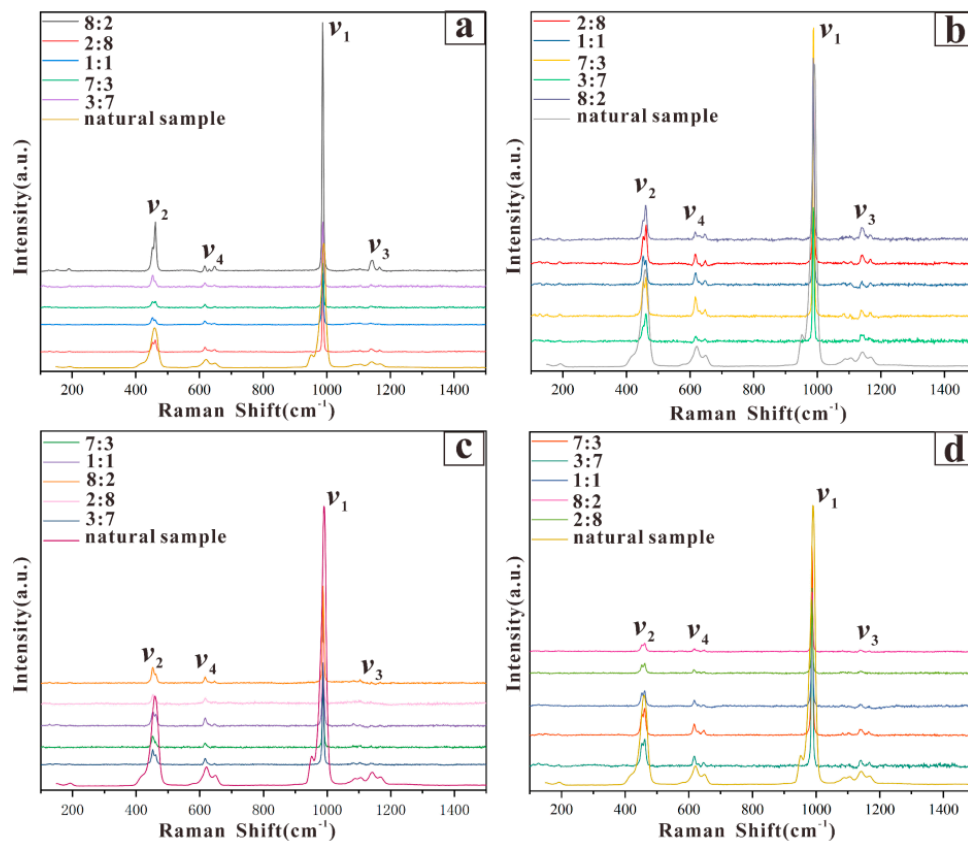


Figure 6. Raman spectra of barite synthesized by mixed solutions at room temperature and in-situ mixes of Na_2SO_4 and BaCl_2 solutions at 200 °C and a natural sample (RRUFFID = R050375). ν_1 , ν_2 , ν_3 , and ν_4 are assigned to the vibrational modes of the SO_4 tetrahedron. (a) Synthesized at 200 °C with 0.03 mol/kg Na_2SO_4 and BaCl_2 solutions, (b) Synthesized at 200 °C with 0.1 mol/kg Na_2SO_4 and BaCl_2 solutions, (c) Synthesized at room temperature with 0.03 mol/kg Na_2SO_4 and BaCl_2 solutions, (d) Synthesized at room temperature with 0.1 mol/kg Na_2SO_4 and BaCl_2 solution. All proportions are molar ratios of Na_2SO_4 and BaCl_2 solutions.

Table 3. Observed Raman vibrational modes (in cm^{-1}) of synthesized barite.

a	This Study				[31,32]	Mode Assignment
	b	c	d			
453	453	452	453	453	$\nu_2 \text{ SO}_4$	
462	461	461	462	463	$\nu_2 \text{ SO}_4$	
618	616	617	616		$\nu_4 \text{ SO}_4$	
622	624	622	622	623	$\nu_4 \text{ SO}_4$	
649	647	646	647	647	$\nu_4 \text{ SO}_4$	
988	988	989	987	988	$\nu_1 \text{ SO}_4$	
1083	1084	1084	1083	1083	$\nu_3 \text{ SO}_4$	
1103	1104	1104	1104	1105	Unassigned	
1139	1138	1139	1138		$\nu_3 \text{ SO}_4$	
1166	1167	1168	1167	1167	$\nu_3 \text{ SO}_4$	

Notes: a. Barite synthesized from 0.03 mol/kg Na_2SO_4 and BaCl_2 solutions with a mixing ratio of 8:2 at 200 °C; b. Barite synthesized by 0.1 mol/kg Na_2SO_4 and BaCl_2 solution with mixing ratio of 7:3 at 200 °C; c. Barite synthesized by 0.03 mol/kg Na_2SO_4 and BaCl_2 solution with mixing ratio of 1:1 at room temperature; d. Barite synthesized by 0.1 mol/kg Na_2SO_4 and BaCl_2 solution with a mixing ratio of 7:3 at room temperature.

The Raman spectra of barite synthesized in these experiments are all similar. Moreover, changes in initial ion concentrations, mixing ratios, and temperature do not change from the positions of characteristic peaks of barite at room temperature (Figure 6). The characteristic Raman peak positions of all synthesized barites are basically consistent with the characteristic peak positions of the pure barite Raman spectrum, and there are no other miscellaneous/unknown peaks. Therefore, Raman hasn't detected any impurities.

3.4. Powder XRD

Although the temperatures, concentrations, and mixing ratios are different, the 2θ of the main peak of barite synthesized in our experiments are basically the same as those of the standard barite. Figure 7 shows representative XRD patterns of barites synthesized at room temperature and 200 °C with an initial concentration of 0.03 mol/kg Na_2SO_4 and BaCl_2 and a mixing ratio of 1:1. The cell parameters of barite synthesized at 200 °C are basically the same as those of barite synthesized at room temperature. The cell parameters of barite synthesized at 200 °C and room temperature are $a = 0.8889$ nm, $b = 0.5454$ nm, and $c = 0.7160$ nm and $a = 0.8884$ nm, $b = 0.5445$ nm, and $c = 0.7156$ nm, respectively, all in good agreement with standard barite ($a = 0.8884$ nm, $b = 0.5456$ nm, and $c = 0.7157$ nm, PDF#83-2053).

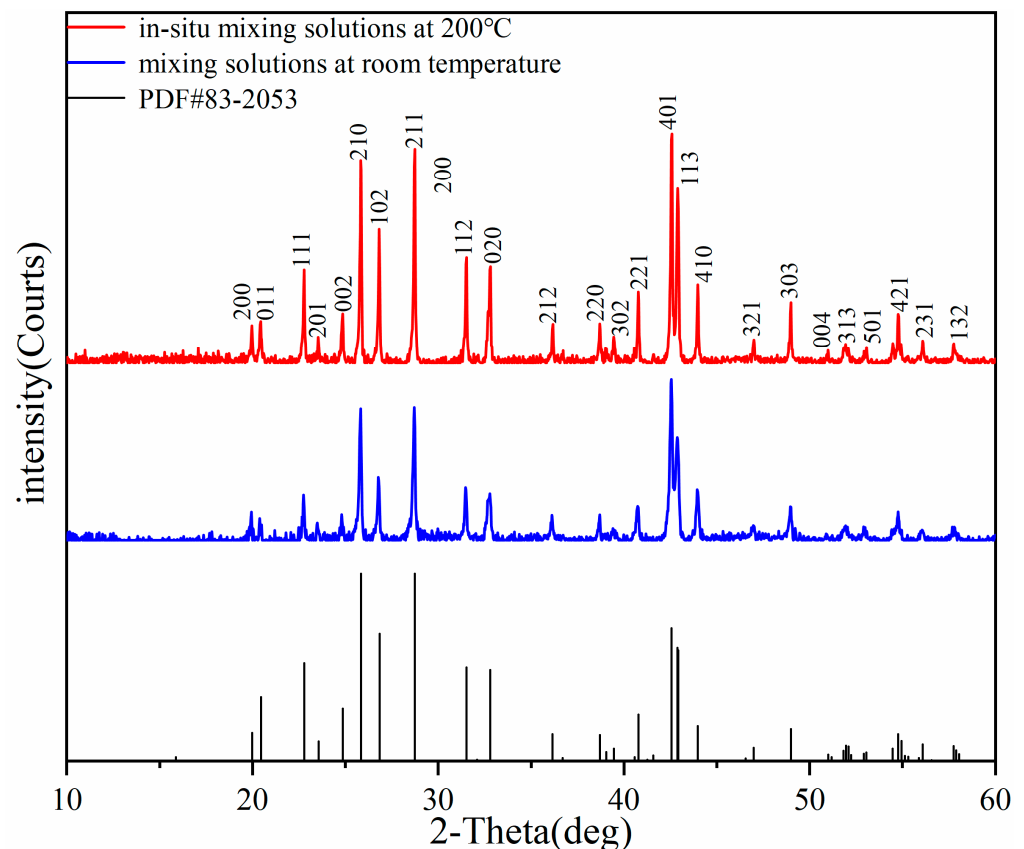


Figure 7. XRD diffractograms of barite synthesized by mixed solution at room temperature and in-situ mixing at 200 °C with an initial concentration of 0.03 mol/kg Na_2SO_4 and BaCl_2 and a mixing ratio of 1:1, along with that of standard barite (PDF#83-2053).

4. Discussion

4.1. The Effect of Temperature on the Morphology of Barite

Temperature is the key factor affecting the morphology of barite. At elevated temperatures, with all other reaction conditions the same, the morphology of the synthesized barites is different. In this study, the morphology of barite synthesized by mixing solutions at room temperature is relatively simple, which is granular or leaf-like (Figure 4). When the concentration of Na_2SO_4 and BaCl_2 solution is 0.03 mol/kg, barite is leaf-like, and when the concentrations of Na_2SO_4 and BaCl_2 solution are 0.1 mol/kg, barite crystals are small and granular. The morphology of the barite synthesized at 25 °C in a previous study [33] is similar to that of leafy barite synthesized at room temperature in this study. Barites synthesized at 150 °C by using barium chloride solutions and native sulfur have the morphologies of rod-shaped and X-shaped [10]. Barites synthesized in this study by in-situ mixing of Na_2SO_4 and BaCl_2 solutions at 200 °C show six different morphologies, including rod, granular, plate, dendritic, X-shaped, T-shaped crystals, while barites synthesized by mixing barium solutions and sulfate solutions at room temperature and subsequent heating to 200 °C, show near-equiaxed granular crystals of well-developed crystal forms [34]. Therefore, the morphologies of barites change from small granular and leaf-like at 25 °C to rod-shaped and X-shaped at 150 °C, and rod, granular, plate, dendritic, X-shaped, T-shaped crystals at 200 °C, which shows the key control of the morphology of barite is temperature.

4.2. Effect of Solution Mixing Ratio on the Morphology of Barite

Precipitation of barite occurs when the product of concentrations of Ba^{2+} and SO_4^{2-} solutions exceed the solubility constant [35]. Varying ionic ratios might be an effective and rather simple way of achieving a degree of crystal morphology control [33,36].

In this study, different solution mixing ratios change the dominant morphology of barite (Table 4). When the concentration of Na_2SO_4 and BaCl_2 solution is 0.03 mol/kg, the dominant morphology of barite with mixing ratios of 8:2 and 2:8 is rod-shaped, the dominant morphology of barite with a mixing ratio of 7:3 is T-shaped, and the dominant morphology of barite with mixing ratios of 1:1 and 3:7 is granular. However, when the initial concentration of Na_2SO_4 and BaCl_2 in solution increases from 0.03 mol/kg to 0.1 mol/kg, the dominant morphology of barite is rod-shaped regardless of the mixing ratio. In addition, when the mixing ratios of Ba^{2+} to SO_4^{2-} solutions with the same concentration is greater than 7:3, the average particle size is increased (Figure 8).

Table 4. Dominant morphology of barite synthesized by in-situ mixing of Na_2SO_4 and BaCl_2 solutions with different concentrations and mixing ratios at 200 °C.

Synthetic Condition		Dominant Morphology
Initial Reactant Concentration	Solution Mixing Ratio ($\text{SO}_4^{2-}/\text{Ba}^{2+}$, Molar Ratio)	
0.03 mol/kg Na_2SO_4 and BaCl_2	8:2	28.2% rod-shaped
	7:3	29.6% T-shaped
	1:1	50.7% granular
	3:7	32.8% granular
	2:8	41.2% rod-shaped
0.1 mol/kg Na_2SO_4 and BaCl_2	8:2	43.5% rod-shaped
	7:3	37.7% rod-shaped
	1:1	61.7% rod-shaped
	3:7	45.8% rod-shaped
	2:8	55.4% rod-shaped

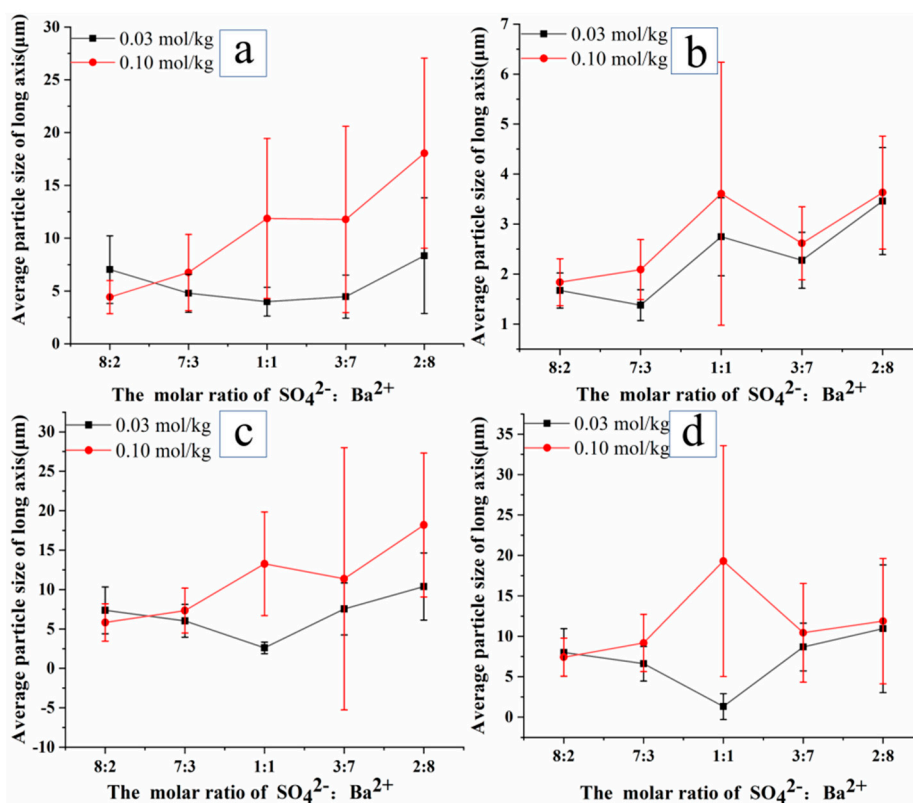


Figure 8. Average particle size of barite synthesized with different initial concentration solution and mixing ratio at 200 °C. (a) rod-shaped (b) granular (c) T-shaped (d) X-shaped.

For barite synthesized by mixing Na_2SO_4 and BaCl_2 solutions with the same concentration at room temperature, the morphology does not change with the initial solution mixing ratio (Figure 4).

4.3. Effect of Supersaturation on the Morphology of Barite

In many kinetic studies of precipitation, it was found that one of the key parameters for characterizing reacting systems is the supersaturation, S . In the case of barite, the supersaturation can be written as [37]:

$$S = \frac{a(\text{Ba}^{2+}) \cdot a(\text{SO}_4^{2-})}{K_{sp}}$$

where $a(\text{Ba}^{2+})$ and $a(\text{SO}_4^{2-})$ are the activities of Ba^{2+} and SO_4^{2-} , respectively, K_{sp} is the solubility product of barite. For barite, K_{sp} is 9.82×10^{-11} at 25 °C [8]. Previous work has demonstrated that at high reagent supersaturation ratios (the natural logarithm of supersaturation ratio, $\ln S = 16.97$), a large number of very small spherical nanoparticles will be formed. At low reagent concentrations ($\ln S = 13.75$), the leaf-like products will be formed [37]. Our experimental results are consistent with the previous research results. In our experiments, when the concentrations of Na_2SO_4 and BaCl_2 are 0.03 mol/kg, barite is leaf-like, and at concentrations of Na_2SO_4 and BaCl_2 are 0.1 mol/kg, barite is small and granular.

At 200 °C, the solubility product of barite is 4×10^{-10} [38], which is larger than that at room temperature. Further, the degree of supersaturation with respect to barite can be changed by varying the barium chloride or sodium sulfate solution concentrations [33]. Dendritic crystals with rough surfaces formed from solutions of high barium chloride concentrations [39]. In our research, dendritic barite was also synthesized when the concentration of barium chloride was high.

Figure 8 shows that although the synthesis temperature and the initial ratios are the same, the particle size of the synthesized barite varies with the initial concentration of Na_2SO_4 and BaCl_2 in the solution. With increasing ion concentration, barite particle sizes increase, indicating a positive correlation between the initial concentration of Na_2SO_4 and BaCl_2 solution and the particle size of the synthesized barite. At 0.1 mol/kg Na_2SO_4 and BaCl_2 in solution, the average particle size of rod-shaped and T-shaped barite crystals increase, while the largest granular and X-shaped barite crystals, form in mixing ratios of 1:1. As plate-shaped and dendritic morphologies only form in mixtures of Na_2SO_4 : $\text{BaCl}_2 = 1:1$ and 2:8, there is no comparison here. Table 4 shows the dominant morphology of barite changing when other reaction conditions are held constant (except for concentration). For example, at higher initial concentrations of Na_2SO_4 and BaCl_2 , the dominant morphology of barite at the mixing ratio of 1:1 and 3:7 changes from granular to rod-like crystal (Table 4). Furthermore, at initial concentrations of Na_2SO_4 and BaCl_2 of 0.03 mol/kg, dendritic barite only appears at mixing ratios of 2:8. However, dendritic barite appears when the concentration of Na_2SO_4 and BaCl_2 increases to 0.1 mol/kg and the mixing ratio is 3:7 (Table 2), indicating that increasing Ba^{2+} concentration favors the formation of dendritic barite.

4.4. Morphological Development of Barite

The morphological development of barite growing in solution is a complicated process. Previous studies indicate that the final morphology of barite depends on the competition of nucleation and crystal growth at different supersaturation ratios [37]. Moreover, the growth of crystals mainly depends on the growth conditions [40,41]. At lower reagent concentrations, homogeneous nucleation generates numerous nanoparticles, while the growth and heterogeneous nucleation of the particles forms bridges to connect the particles, forming leaf-like crystals [37]. However, at high reagent supersaturation ratios, a short nucleation burst leads to the production of abundant spherical nanoparticles, which exhausts most of the reagent and limits the further growth of particles [42]. The morphological development of barite synthesized at room temperature in this study is consistent with this scenario (Figure 4).

However, the development of the morphology of barite formed by in-situ mixing BaCl_2 and Na_2SO_4 solutions at 200 °C is more complicated. When mixing in situ at high temperatures, the nucleation and growth of barite occur simultaneously. There is no time to produce perfect crystal nuclei, and supersaturation in the environment around the crystal nucleus is high, so crystal nuclei tend to grow randomly, forming abundant defects. At these defect points, the crystal lattice is disturbed, and new layers begin growing [43]. Moreover, at higher temperatures the fluid state is unstable, and the atomic thermal vibration is strong, so Ba^{2+} and SO_4^{2-} ions can obtain enough energy to overcome the fluid resistance and migrate rapidly. As a result, a wide variety of shapes form, including rod-shaped, granular, plate-shaped, dendritic, X-shaped, and T-shaped.

Moreover, the dendritic barite synthesized by in-situ mixing of 0.03 mol/kg Na_2SO_4 and BaCl_2 at mixing ratios of 2:8 and 0.1 mol/kg Na_2SO_4 and BaCl_2 at mixing ratios of 3:7 and 2:8 at 200 °C is very special. The diffusion-limited aggregation model is usually used to explain the formation of such dendritic crystals [40,41]. The core idea of the diffusion-limited aggregation model is that crystal growth is mainly limited by diffusion. During crystal growth, the surrounding growth points diffuse toward the center and "adhere" to the growth center, and all the particles that can diffuse to the crystal nucleus can grow continuously, thus forming a branching epitaxy and dendritic crystal [44]. According to the diffusion-limited aggregation model, the formation process of dendritic barite by in-situ mixing of BaCl_2 and Na_2SO_4 solutions at mixing ratios of 3:7 and 2:8 at 200 °C can be briefly described as follows (Figure 9).

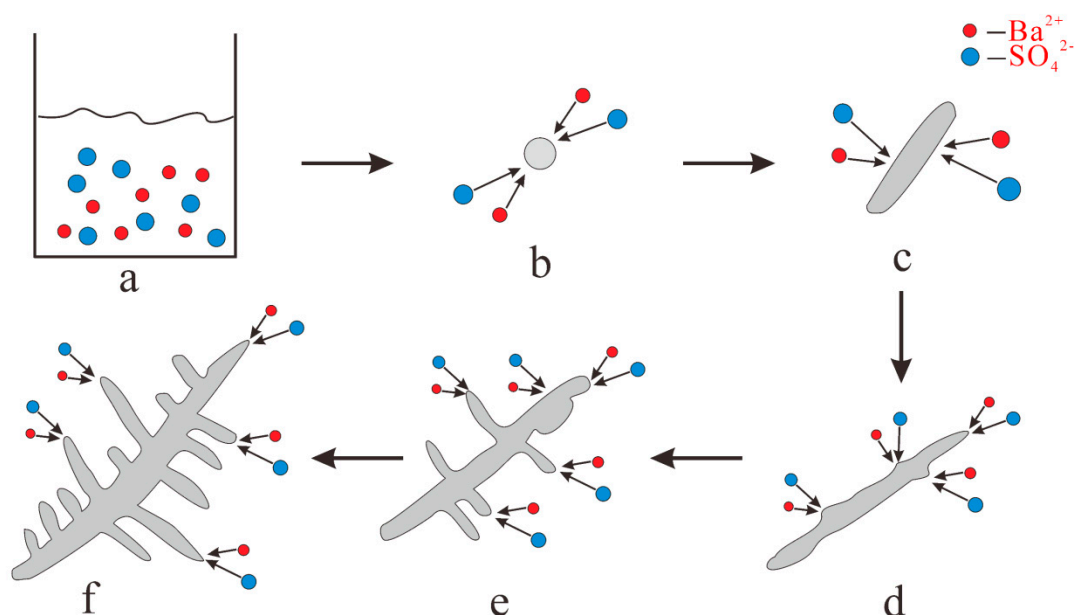


Figure 9. A schematic diagram of the formation of dendritic barite at high temperature. (a) Mixed solutions of sodium sulfate and barium chloride; (b) Granular barite; (c) Rod barite; (d) develops fine branches; (e) Branches continue to develop; (f) Dendritic barite.

It is well known that dendritic growth occurs under non-equilibrium conditions leading to morphologies that are not necessarily the most stable in terms of surface energy [45,46]. Due to the high ambient temperature of the crystal nucleus, the unstable fluid state, the strong thermal vibration of atoms, and the high Ba^{2+} concentrations, some crystal nuclei may preferentially grow. Therefore, granular crystals first develop into rod-like crystals (Figure 9b,c). With the progress of growth, on the one hand, the rod-shaped crystals grow along the long axis of the column, however, agglomeration points due to the high local concentration will be formed at some positions on the column surface [47]. Then agglomeration points on the column surface of the rod-shaped barite gradually uplift (Figure 9d). As the nanocrystals continue to gather and grow, new growth fronts are created. Consequently, overgrowth occurs in the new growth front and branches gradually develop on the sides (Figure 9e). Finally, in a manner similar to growth patterns of trees, overgrowth occurs at some point on the branch, resulting in the formation of dendritic barite (Figure 9f).

4.5. Geological Implications

The formation and evolution of seafloor hydrothermal vents are often accompanied by barite precipitation [19]. On the seafloor, heat generated by deep magmatic activity drives seawater circulation along mid-ocean ridges, island arcs, and back-arc basins [48]. When the fluids circulate, heated fluids react with the surrounding rock, and vent onto the seafloor, forming hydrothermal chimneys and mounds. Where hydrothermal fluids are discharged, the mixing of hydrothermal fluids with the surrounding seawater drives mineral precipitation [49]. The outer wall of this porous chimney contains a typical series of low-temperature minerals (sphalerite, barite, etc.), which is formed by hydrothermal fluid cooling and/or mixing with seawater [50]. The precipitation of barite is formed by the mixture of Ba^{2+} in hydrothermal fluid and SO_4^{2-} in seawater [35].

Various forms of barite form in hydrothermal vents at Endeavour, from well-formed tabular and bladed crystals to dendritic crystals [19]. Dendritic barite forms where the outer wall of the nozzle is in contact with the seawater, which is very similar to the barite synthesized by in-situ mixing of BaCl_2 and Na_2SO_4 solutions at 200 °C in this study. Temperature measurements of fluid inclusions in barite from hydrothermal vents show formation temperatures of pressure-corrected inclusions are 180–240 °C, which is also close

to the experimental temperature (200 °C) in this study. Combined with field observations and our experimental results, it is concluded that dendritic structures may be an important morphological feature of barite formed by in-situ mixing of seafloor hydrothermal solutions at high temperatures.

However, the mixing ratio of Na_2SO_4 and BaCl_2 solutions for dendritic barite formation in our experiment are not exactly the same as that for dendritic barite formation in the hydrothermal vent at Endeavour. The dendritic barite is believed to be formed by mixing of Ba^{2+} -bearing hydrothermal fluids with the SO_4^{2-} -bearing surrounding seawater with a mixing ratio of 4:6 at 180–240 °C in hydrothermal vents at Endeavour [19]. In our experiments, the dendritic barite only occurred under the conditions of excess Ba^{2+} relative to SO_4^{2-} . If we regard Na_2SO_4 and BaCl_2 solutions at 200 °C as SO_4^{2-} rich hot seawater and Ba^{2+} -containing hydrothermal fluid, respectively, more than 80% of the hydrothermal components are needed to form dendritic crystals. This hydrothermal component is much larger than that (40%) estimated in the hydrothermal vent of Endeavour [19], which means that the formation of dendritic barite in natural hydrothermal vents may be affected by other species in the fluids and further researches are needed.

5. Conclusions

Barite of a range of morphologies was synthesized at 200 °C and room temperature by in-situ mixing of BaCl_2 and Na_2SO_4 solutions. The synthesized barite was analyzed by SEM, XRD, and Raman spectroscopy. The main conclusions of this study are as follows:

The temperature has an obvious effect on the morphology of synthesized barite. Barite synthesized by in-situ mixing of BaCl_2 and Na_2SO_4 solutions at 200 °C has rich morphologies, such as rod-shaped, granular, plate-shaped, dendritic, X-shaped, and T-shaped crystals, while the morphology of barite synthesized at room temperature is relatively simple; granular or leaf-like.

When barite was synthesized by in-situ mixing of BaCl_2 and Na_2SO_4 solutions at 200 °C, the morphology of barite is affected by the initial mixing ratio. Dendritic barites will appear when Ba^{2+} is in excess of SO_4^{2-} . In this study, dendritic barite only appeared at $\text{Ba}^{2+}/\text{SO}_4^{2-}$ molar ratios of 8:2 with initial concentrations of Na_2SO_4 and BaCl_2 of 0.03 mol/kg or at $\text{Ba}^{2+}/\text{SO}_4^{2-}$ molar ratios of 8:2 and 7:3 and initial concentrations of Na_2SO_4 and BaCl_2 of 0.1 mol/kg.

Dendritic textures may be an important typomorphic feature of barite formed under the conditions of high-temperature fluid mixing, such as in seafloor hydrothermal systems. Dendritic barite is formed at the contact between the outer wall of the seafloor hydrothermal vent and seawater, which is very similar to the barite synthesized by in-situ mixing of BaCl_2 and Na_2SO_4 solutions at 200 °C in this study.

Author Contributions: Conceptualization, C.W. (Chunyao Wang) and L.Z.; methodology, L.Z.; software, C.W. (Chunyao Wang), S.Z., L.W., C.W. (Chunwan Wei), W.S. and L.X.; validation, C.W. (Chunyao Wang), S.Z., L.W., C.W. (Chunwan Wei), W.S. and L.X.; investigation, C.W. (Chunyao Wang), S.Z., L.W., C.W. (Chunwan Wei), W.S. and L.X.; writing, C.W. (Chunyao Wang), L.Z., and W.Z. All authors have read and agreed to the published version of the manuscript.

Funding: This research was funded by the Natural Science Foundation of China (91962108 and 41773058), the Key Research Program of Frontier Sciences, CAS (QYZDB-SSW-DQC008), EXPRO project of the Czech Science Foundation (No. 19-29124X), and the Research Grant of the Guizhou Normal University (GZNU2019)4.

Data Availability Statement: Not applicable.

Acknowledgments: We thank the Editor and three anonymous reviewers whose comments helped improve and clarify this manuscript. We also thank John Mavrogenes and Terry Mernagh for constructive suggestions that helped improve the manuscript.

Conflicts of Interest: The authors declare no conflict of interest.

References

1. Jewell, P.W. Bedded barite in the geologic record. *Mar. Authigenesis Glob. Microb.* **2000**, *64*, 147–161.
2. Bonny, S.M.; Jones, B. Diatom-mediated barite precipitation in microbial mats calcifying at Stinking Springs, a warm sulphur spring system in Northwestern Utah, USA. *Sediment. Geol.* **2007**, *194*, 223–244. [[CrossRef](#)]
3. Huston, D.L.; Logan, G.A. Barite, BIFs and bugs: Evidence for the evolution of the Earth's early hydrosphere. *Earth Planet. Sci. Lett.* **2004**, *220*, 41–55. [[CrossRef](#)]
4. Senko, J.M.; Campbell, B.S.; Henriksen, J.R.; Elshahed, M.S.; Dewers, T.A.; Krumholz, L. Barite deposition resulting from phototrophic sulfide-oxidizing bacterial activity. *Geochim. Cosmochim. Acta* **2004**, *68*, 773–780. [[CrossRef](#)]
5. Bottrell, S.H.; Newton, R.J. Reconstruction of changes in the global sulphur cycling from marine sulphate isotopes. *Earth-Sci. Rev.* **2006**, *75*, 59–83. [[CrossRef](#)]
6. Sanz-Montero, M.E.; Rodríguez-Aranda, J.; Cura, M. Bioinduced precipitation of barite and celestite in dolomite microbialites: Examples from Miocene lacustrine sequences in the Madrid and Duero Basins. *Sediment. Geol.* **2009**, *222*, 138–148. [[CrossRef](#)]
7. Griffith, E.M.; Paytan, A. Barite in the ocean—Occurrence, geochemistry and palaeoceanographic applications. *Sedimentology* **2012**, *59*, 1817–1835.
8. Widanagamage, I.; Waldron, A.; Glamoclija, M. Controls on Barite Crystal Morphology during Abiotic Precipitation. *Minerals* **2018**, *8*, 480. [[CrossRef](#)]
9. Niu, H.; Chen, F. Re-evaluation of the geochemistry of magmatic barite and fluorite. *Acta Mineral. Sin.* **1996**, *16*, 382–388.
10. Niu, H.; Lin, C. The genesis of the mianning rare earth deposit, sichuan province. *Miner. Depos.* **1994**, *013*, 345–353.
11. Bishop, J.K.B. The barite-opal-organic carbon association in oceanic particulate matter. *Nature* **1988**, *332*, 341–343. [[CrossRef](#)]
12. Bertram, M.A.; Cowen, J.P. Morphological and compositional evidence for biotic precipitation of marine barite. *J. Mar. Res.* **1997**, *55*, 577–593. [[CrossRef](#)]
13. Jin, Z.; Zhu, D.; Hu, W.; Zhang, X.; Wang, Y.; Yan, X.B. Geological and geochemical signatures of hydrothermal activity and their influence on carbonate reservoir beds in Tarim Basin. *Acta Geol. Sin.* **2006**, *80*, 245–253.
14. Vandeginste, V.; Stehle, M.C.; Jourdan, A.L.; Bradbury, H.J.; Manning, C.; Cosgrove, J.W. Diagenesis in salt dome roof strata: Barite-calcite assemblage in Jebel Madar, Oman. *Mar. Pet. Geol.* **2017**, *86*, 408–425.
15. Shikazono, N. Genesis of sulfate mineral in the Kuroko deposits. *Min. Geol.* **1983**, *11*, 229–249.
16. Dill, H.; Carl, C. Sr Isotope Variation in Vein Barites from the NE Bavarian Basement: Relevance for the Source of Elements and Genesis of Unconformity-Related Barite Deposits. *Mineral. Petrol.* **1987**, *36*, 27–39. [[CrossRef](#)]
17. Ehya, F. Rare earth element and stable isotope (O, S) geochemistry of barite from the Bijgan deposit, Markazi Province, Iran. *Mineral. Petrol.* **2012**, *104*, 81–93. [[CrossRef](#)]
18. Safina, N.P.; Melekestseva, I.Y.; Nimis, P.; Ankusheva, N.N.; Yuminov, A.M.; Kotlyarov, V.A.; Sadykov, S.A. Barite from the Saf'yanovka VMS deposit (Central Urals) and Semenov-1 and Semenov-3 hydrothermal sulfide fields (Mid-Atlantic Ridge): A comparative analysis of formation conditions. *Miner. Depos.* **2015**, *51*, 491–507. [[CrossRef](#)]
19. John, J.W.; Mark, H.D.; Margaret, K.T.; Thor, H.; Williamson, N.M.; Margaret, S.; Jan, F.; David, B.; Matthias, F.; Leigh, A.; et al. Precipitation and growth of barite within hydrothermal vent deposits from the Endeavour Segment, Juan de Fuca Ridge. *Geochim. Cosmochim. Acta* **2016**, *173*, 64–85.
20. Blount, C.W. Synthesis of barite, celestite, anglesite, witherite, and strontianite from aqueous solutions. *Am. Mineral.* **1974**, *59*, 1209–1219.
21. Liu, S.; Nancollas, G.H. Scanning electron microscopic and kinetic studies of the crystallization and dissolution of barium sulfate crystals. *J. Cryst. Growth* **1976**, *33*, 11–20. [[CrossRef](#)]
22. Rizkalla, E.N. Kinetics of the crystallization of barium sulphate. *J. Chem. Soc. Faraday Trans I* **1983**, *79*, 1857–1867. [[CrossRef](#)]
23. Uchida, M.; Sue, A.; Yoshioka, T.; Okuwaki, A. Hydrothermal synthesis of needle-like barium sulfate using a barium (II)-EDTA chelate precursor and sulfate ions. *J. Mater. Sci. Lett.* **2000**, *19*, 1373–1374. [[CrossRef](#)]
24. Kowacz, M.; Putnis, C.V.; Putnis, A. The effect of cation:anion ratio in solution on the mechanism of barite growth at constant supersaturation: Role of the desolvation process on the growth kinetics. *Geochim. Cosmochim. Acta* **2007**, *71*, 5168–5179. [[CrossRef](#)]
25. Ray, D.; Kota, D.; Das, P.; Prakash, S. Microtexture and distribution of minerals in hydrothermal barite-silica chimney from the franklin seamount, sw pacific: Constraints on mode of formation. *Acta Geol. Sin. Engl. Ed.* **2014**, *88*, 213–225.
26. Aymonier, C.; Cansell, F.; Mecking, S.; Moisan, S.; Martinez, V. Synthesis of Particles in Dendritic Structures. U.S. Patent 7,932,311, 26 April 2011.
27. Martin, S.; Espen, D.B.; Mogens, C.; Iversen, B. Size and Morphology Dependence of ZnO Nanoparticles Synthesized by a Fast Continuous Flow Hydrothermal Method. *Cryst. Growth Des.* **2011**, *11*, 4027–4033.
28. Diez-Garcia, M.; Gaitero, J.J.; Dolado, J.S.; Aymonier, C. Ultra-Fast Supercritical Hydrothermal Synthesis of Tobermorite under Thermodynamically Metastable Conditions. *Angew. Chem.* **2017**, *129*, 3210–3215. [[CrossRef](#)]
29. Miyake, M.; Minato, I.; Morikawa, H.; Iwai, S. Crystal structures and sulphate force constants of barite, celestite, and anglesite. *Am. Mineral.* **1978**, *63*, 506–510.
30. Ross, S.D. Inorganic infrared and raman spectra. *J. Mol. Struct.* **1973**, *15*, 468–469.
31. Griffith, W.P. Raman studies on rock-forming minerals. Part II. Mineral containing MO₃, MO₄, and MO₆ groups. *J. Chem. Soc.* **1970**, 286–291. [[CrossRef](#)]
32. Griffith, W.P. Advances in the Raman and Infrared spectroscopy of minerals. *Adv. Spectrosc.* **1987**, *14*, 119–186.

33. Wong, D.C.Y.; Jaworski, Z.; Nienow, A.W. Effect of Ion Excess on Particle Size and Morphology during Barium Sulphate Precipitation: An Experimental Study. *Chem. Eng. Sci.* **2001**, *56*, 727–734. [[CrossRef](#)]
34. Wang, L.; Zhou, L.; Zhang, S.; Wang, C.; Zhou, W. Hydrothermal synthesis of barite using the in-situ high temperature mixing method. *Acta Mineral. Sin.* **2021**, *41*, 139–149.
35. Blount, C.W. Barite solubilities thermodynamic and quantities up to 300 °C and 1400 bars. *Am. Mineral.* **1977**, *62*, 942–957.
36. Zhang, H.; Zhu, L.; Chen, J.; Chen, L.; Liu, C.; Yuan, S. Morphologically Controlled Synthesis of Cs₂SnCl₆ Perovskite Crystals and Their Photoluminescence Activity. *Crystals* **2019**, *9*, 258. [[CrossRef](#)]
37. Li, S.; Xu, J.; Luo, G. Control of crystal morphology through supersaturation ratio and mixing conditions. *J. Cryst. Growth* **2007**, *304*, 219–224. [[CrossRef](#)]
38. Strtibel, G. Zur Kenntnis und genetischen Bedeutung des Systems BaSO₄-NaCl-H₂O. *Neues Jahrb. Mineral. Mon.* **1967**, *4*, 223–234.
39. Shikazono, N. Precipitation mechanisms of barite in sulfate-sulfide deposits in back-arc basins. *Geochim. Cosmochim. Acta* **1994**, *58*, 2203–2213. [[CrossRef](#)]
40. Paul, M. Formation of fractal clusters and networks by irreversible diffusion-limited aggregation. *Phys. Rev. Lett.* **1983**, *51*, 1119–1122.
41. Sander, L.M. Diffusion-Limited Aggregation, a Kinetic Critical Phenomenon. *Contemp. Phys.* **2000**, *41*, 203–218. [[CrossRef](#)]
42. Murray, C.B.; Kagan, C.R.; Bawendi, M.G. Synthesis and characterization of monodisperse nanocrystals and close-packed nanocrystal assemblies. *Annu. Rev. Mater. Sci.* **2000**, *30*, 545–610. [[CrossRef](#)]
43. Judat, B.; Kind, M. Morphology and internal structure of barium sulfate—derivation of a new growth mechanism. *J. Colloid Interface Sci.* **2004**, *269*, 341–353. [[CrossRef](#)]
44. Huang, Q.; Zhao, S. Development of dentrite study. *J. Synth. Cryst.* **2002**, *31*, 486.
45. Chernov, A.A.; Lewis, J. computer model of crystallization of binary systems; kinetic phase transitions. *J. Phys. Chem. Solids* **1967**, *28*, 2185–2198. [[CrossRef](#)]
46. Kobayashi, T.; Kuroda, T. *Morphology of Crystals*; Sunagawa, I., Ed.; Terra Scientific Publishing: Tokyo, Japan, 1987.
47. Angerhöfer, M. Untersuchungen zur Kinetik der Fällungskristallisation von Bariumsulfat. Ph.D. Thesis, Technical University Munich, Munich, Germany, 1995.
48. Baker, E.T.; German, C.R.; Elderfield, H. Hydrothermal Plumes over Spreading-Center Axes: Global Distributions and Geological Inferences. *Am. Geophys. Union* **1995**, *91*, 47–71.
49. Hannington, M.D.; Jonasson, I.R.; Herzig, P.M.; Petersen, S. Physical and chemical processes of seafloor mineralization at mid-ocean ridges. *Seafloor Hydrotherm. Syst. Phys. Chem. Biol. Geol. Interact.* **1995**, *91*, 115–157.
50. Tivey, M.K.; Stakes, D.S.; Cook, T.L.; Hannington, M.D.; Petersen, S. A model for growth of steep-sided vent structures on the Endeavour Segment of the Juan de Fuca Ridge: Results of a petrologic and geochemical study. *J. Geophys. Res. Solid Earth* **1999**, *104*, 22859–22883. [[CrossRef](#)]